Applied Catalysis B: Environmental 185 (2016) 353–361

Contents lists available at ScienceDirect

Applied Catalysis B: Environmental

journal homepage: www.elsevier.com/locate/apcatb

Fe-silicalites as heterogeneous Fenton-type catalysts for radiocobalt removal from EDTA chelates

Kseniya A. Sashkina[a,b,d,*], Alexander V. Polukhin[a,b,*], Vera S. Labko[c], Artem B. Ayupov[a], Anton I. Lysikov[a,b,d], Ekaterina V. Parkhomchuk[a,b,d,*]

[a] Boreskov Institute of Catalysis SB RAS, 5 Lavrentieva st., Novosibirsk 630090, Russia
[b] Research and Education Centre, NSU, 2 Pirogova st., Novosibirsk 630090, Russia
[c] State Scientific Institution "The Joint Institute for Power and Nuclear Research—Sosny", 99 Academician A.K. Krasin Str., Minsk BY-220109, Belarus
[d] Novosibirsk State University, 2 Pirogova st., Novosibirsk 630090, Russia

ARTICLE INFO

Article history:
Received 23 September 2015
Received in revised form 1 December 2015
Accepted 18 December 2015
Available online 23 December 2015

Keywords:
Hierarchical zeolite
Heterogeneous Fenton-type catalyst
Fe-silicalite
EDTA oxidation
Radiocobalt removal

ABSTRACT

Fe-silicalite nano- and microcrystals as heterogeneous Fenton-type catalysts have been synthesized and characterized by dynamic light scattering, X-ray diffraction, scanning and transmission electron microscopy, nitrogen adsorption measurements, inductively coupled plasma optical emission spectrometry, UV visible diffuse reflectance spectroscopy and temperature-programmed desorption of ammonia. Catalytic performance of Fe-silicalites was studied in mineralization of EDTA by H_2O_2 at 303–353 K and ^{60}Co removal from EDTA chelates. The effect of activation by the acid treatment on the state of active sites, catalytic activity and stability of Fe-silicalites was studied. Fe-silicalites nanocrystals are more efficient catalysts *vs.* microcrystals due to enhanced catalytic sites accessibility.

1. Introduction

Complexing agents including ethylenediaminetetraacetic acid (EDTA), aminotris (methylenephosphonic) acid (ATMP), 1-hydroxyethylidene-bisphosphonic acid (HEDP), citric and oxalic acids are used at nuclear power plants for decontaminating the reactors due to their ability to form strong complexes with radioactive metals. The key problem of the liquid radioactive waste treatment is the complicated sorption and precipitation of chelated radionuclides, especially strong ^{60}Co chelates with EDTA (the stability constants for Co(II) and Co(III) complexes with EDTA equals 10^{-16} and 10^{-40}, respectively). The treatment of liquid radioactive wastes followed by their concentrating becomes easier after the destruction of chelates. There are different methods for the complexing agent's removal including chemical [1–5] and electrochemical oxidation [6,7]. Environmentally friendly advanced oxidation processes (AOPs) based on •OH-radicals generation at ambient conditions for EDTA destruction having been also developing: photocatalytic oxidation [8,9], hydrogen peroxide photo-assisted processes [10], homogeneous Fenton and photo-Fenton systems [11–14], ozonation and UV-assisted ozonation [15].

We suggest a new method of radiocobalt removal from EDTA chelates by catalytic oxidation of EDTA by H_2O_2 *via* heterogeneous Fenton-type zeolite catalysts. Zeolites are crystalline silicates and aluminosilicates linked through oxygen atoms, producing a three-dimensional network containing channels and cavities of molecular dimensions [16].

The present study describes the synthesis of Fe-silicalite nano- and microcrystals as catalysts. Effect of the activation by acid treatment on catalytic activity and stability of Fe-silicalites can be found below. Interplay between the crystal size of Fe-silicalites and both total EDTA oxidation and radiocobalt removal efficiencies are shown.

measurement conditions (Table 1

2. Materials and methods

2.1. Reagents

Tetrapropylammonium hydroxide (TPAOH, 25 wt.% solution in water, Acros), tetrapropylammonium bromide (98%, Aldrich), tetraethylorthosilicate (TEOS, ≥98%, Angara-reactive, silica)

* Corresponding authors at: Boreskov Institute of Catalysis SB RAS, 5 Lavrentieva st., Novosibirsk 630090, Russia.
E-mail address: sashkina@catalysis.ru (K.A. Sashkina).

http://dx.doi.org/10.1016/j.apcatb.2015.12.038
0926-3373/

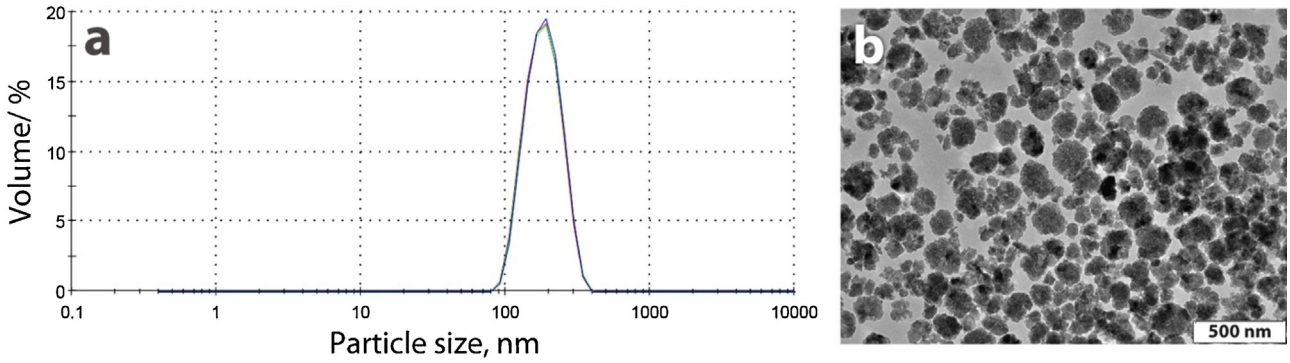

Fig. 1. Dynamic light scattering data for Fe-silicalite suspension (a) and TEM image of Fe-silicalite nanocrystals (b).

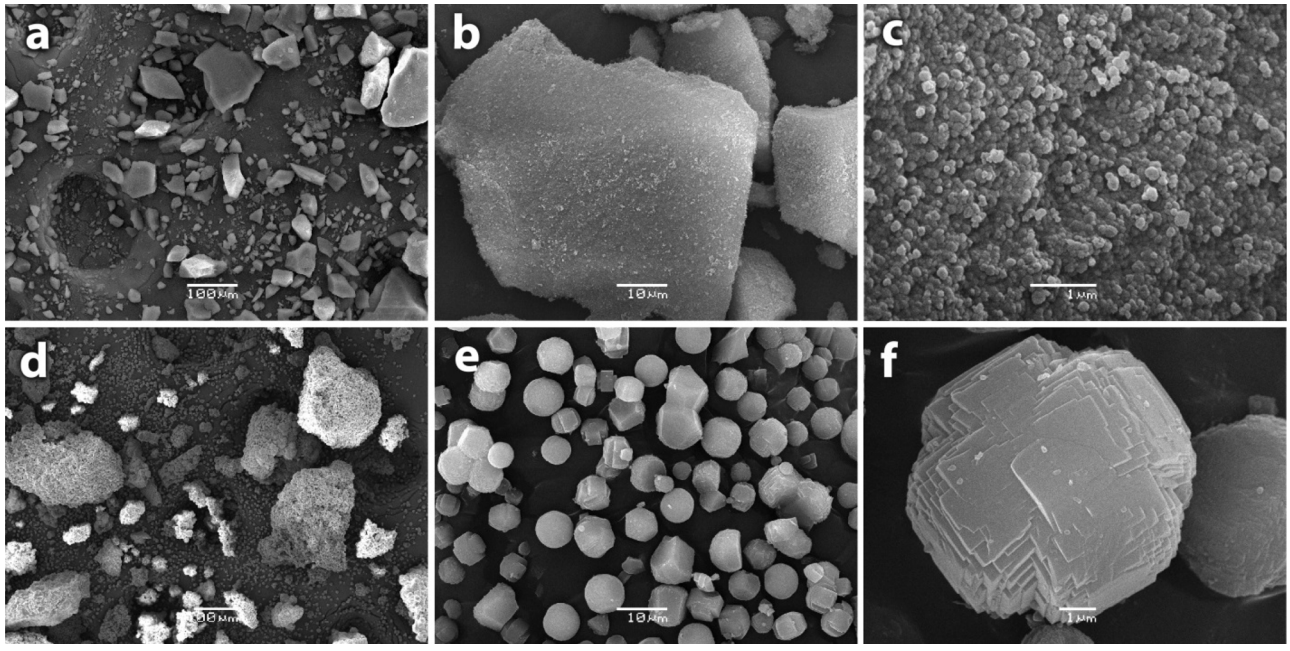

Fig. 2. SEM images of calcined Fe-silicalite nanocrystals at different magnifications with scale bars of 100 μm (a), 10 μm (b) and 1 μm (c), as well as Fe-silicalite microcrystals with scale bars of 100 μm (d), 10 μm (e) and 1 μm (f).

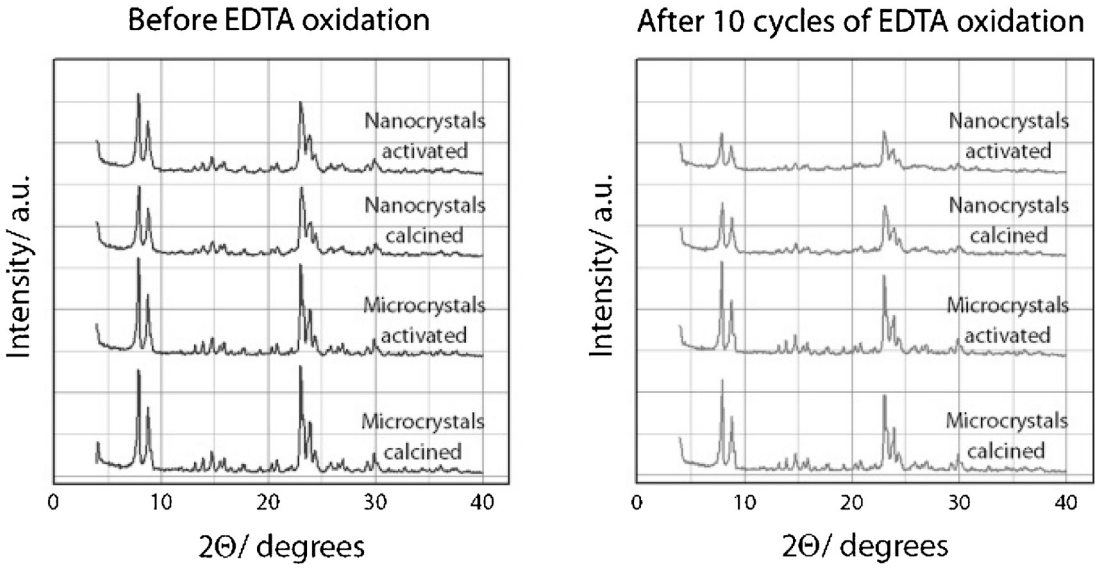

Fig. 3. XRD patterns of Fe-silicalites.

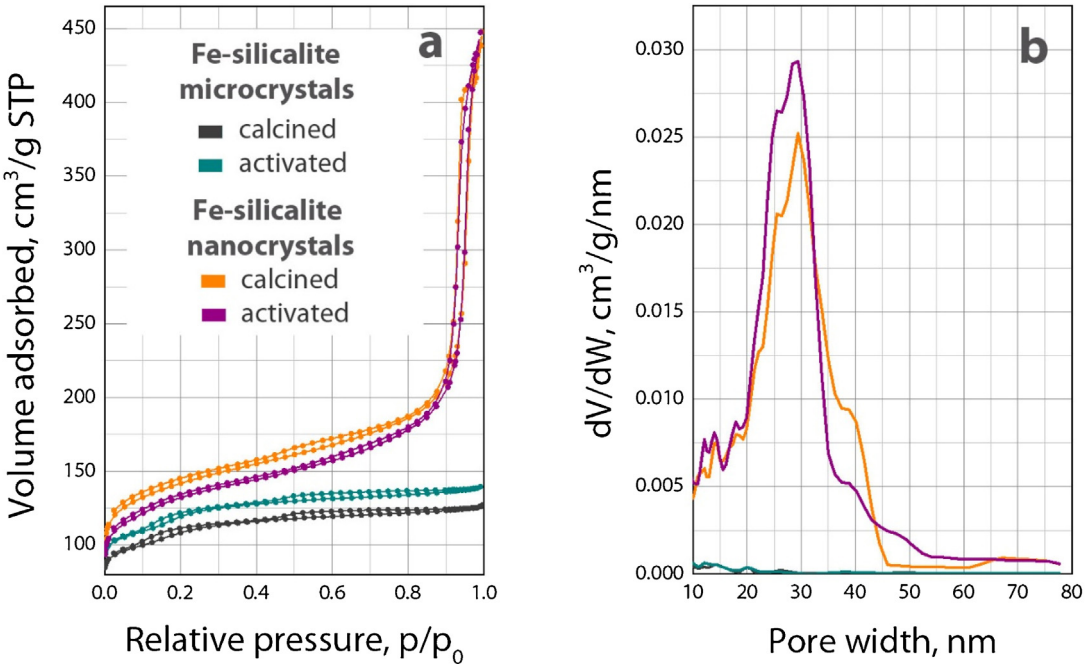

Fig. 4. Nitrogen adsorption/desorption isotherms (a) and mesopore size distributions (b) of calcined Fe-silicalites.

Table 1
Physicochemical properties of Fe-silicalite catalysts.

Fe-silicalite sample	S_{BET}, m^2/g	S_{Ext}, m^2/g	V_{total}, cm^3/g	V_{micro}, cm^3/g	XRD crystallinity, %		Fe content, wt.%			Total NH_3 adsorption capacity, mmol/g
					Before EDTA oxidation	After 10 cycles of EDTA oxidation	The catalytic cycle			
							0	5	10	
Microcrystals calcined	398	107	0.19	0.12	100	85	1.42	1.31	1.25	0.11
Microcrystals activated	437	117	0.22	0.13	94	85	1.42	1.16	1.19	0.17
Nanocrystals calcined	524	234	0.68	0.12	96	80	1.32	1.24	1.12	0.15
Nanocrystals activated	480	205	0.69	0.11	96	68	1.2	1.09	1.03	0.11

(fumed, ≥99%, Aldrich), ethanol (EtOH, 95%, Pharmaceya) and $Fe(NO_3)_3{\cdot}9H_2O$ (≥99%, Merck) were used for preparing the Fe-silicalites. Oxalic acid ($H_2C_2O_4{\cdot}2H_2O$, Reakhim) was used for the catalysts activation. Hydrogen peroxide (H_2O_2, 30%, Baza No. 1 Khimreaktivov), disodium ethylenediaminetetraacetate (Trilon B, Pyat okeanov), $Co(NO_3)_3{\cdot}6H_2O$ (Reakhim), $^{60}Co(NO_3)_3$ (Amersham International), HNO_3 (13 M, Pyat okeanov) and NaOH (Pyat okeanov) were applied for catalytic experiments.

2.2. Synthesis of Fe-silicalite catalysts

The typical synthesis of Fe-silicalite nanocrystals was carried out as follows. 120 mL of TEOS diluted with 120 mL of ethanol was added at once to 240 mL of TPAOH (12.5 wt.%) under vigorous stirring for 20 min, then 2.6 g of $Fe(NO_3)_3{\cdot}9H_2O$ dissolved in 5 mL of distilled water was added dropwise. After stirring for 20 min, the resultant clear light-yellow gel with 1.00 SiO_2: 0.28 TPAOH: 0.006 Fe_2O_3: 4.79 EtOH: 1.75H_2O molar composition was placed in Teflon-lined stainless steel autoclaves and subjected to hydrothermal treatment in an oven at 363 K for 7 days. Milky Fe-silicalite suspension produced was purified in a series of three steps consisting of centrifugation at relative acceleration of $3000 \times g$ for 5 h, followed by removal of the mother liquor and redispersion in distilled water under ultrasonification. Purified Fe-silicalite was separated by centrifugation, dried at 323 K for 12 h.

The synthesis of large Fe-silicalite microcrystals was performed at the following chemical composition of the precursor solution: 1.00 SiO_2: 0.1 Na_2O: 0.11 TPABr: 0.006 Fe_2O_3: 25H_2O. In a typical synthesis procedure, 40 g of silica was gradually added to an aqueous solution containing 5.36 g NaOH and 19.5 g of TPABr under magnetic stirring at ambient temperature. After stirring for 15 min, 3.2 g of $Fe(NO_3)_3{\cdot}9H_2O$ dissolved in 5 mL of distilled water was added dropwise to obtained milky suspension. After further stirring for 10 min, the gel mixture was transferred to a Teflon-lined stainless steel autoclave. The autoclave was maintained in an oven at 433 K for 72 h. After the hydrothermal treatment, the solid product was filtered, rinsed with distilled water and dried at 373 K for 12 h.

0.5 g of each Fe-silicalite was left in the initial as-synthesized form. The rest catalysts were calcined at 773 K for 5 h. One half of calcined Fe-silicalites was left in the calcined form, whereas the other half was activated by acid treatment followed by calcination. For the activation, calcined Fe-silicalites were put in 1 M aqueous solution of oxalic acid with the Fe-silicalite concentration of 100 g L^{-1} and stirred for 30 min at 50 °C. The samples after acid treatment were filtered and rinsed with distilled water until pH 7.0, dried in air at 323 K for 12 h and calcined at 773 K for 3 h to produce the activated form. Fe-silicalite powders were ground in a mortar, and the fractions <200 μm were separated by sifting.

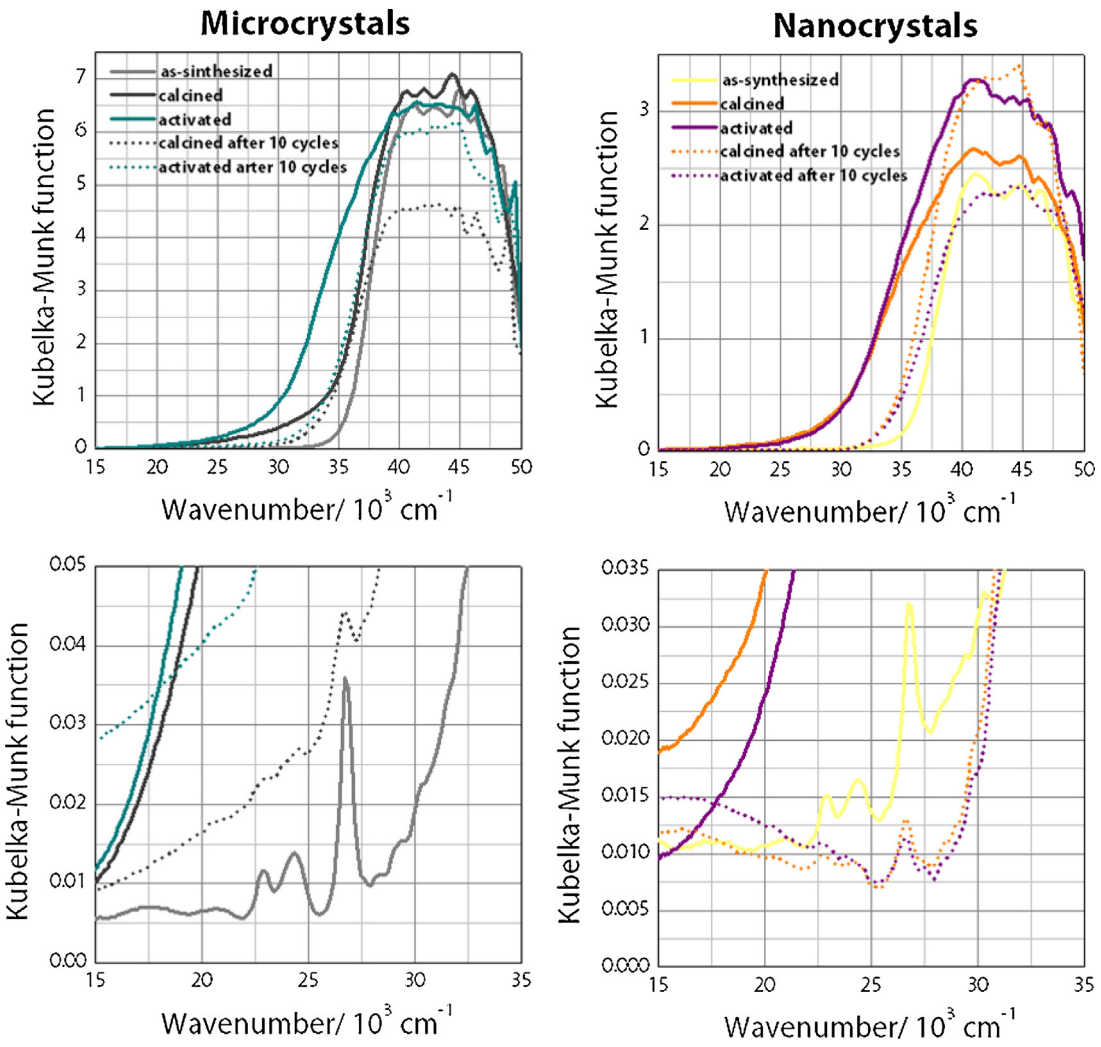

Fig. 5. Ultraviolet-visible diffused reflection spectra of Fe-silicalite nano- and microcrystals.

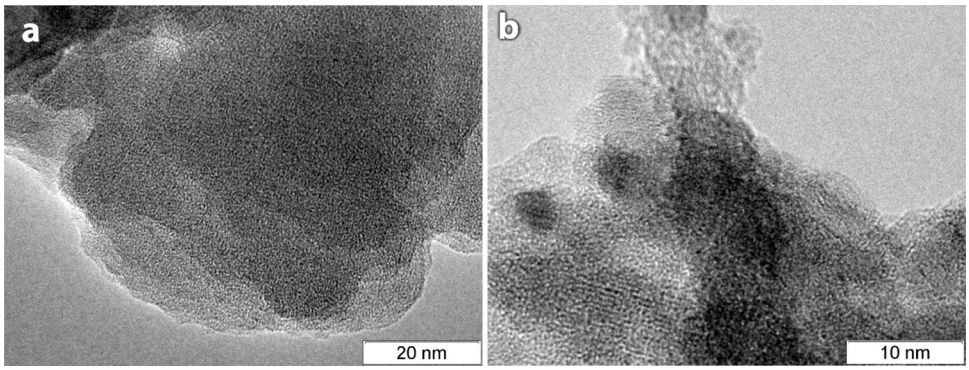

Fig. 6. TEM images of activated Fe-silicalite nanocrystals (a) and microcrystals (b).

2.3. Catalysts characterization

Powder X-ray diffraction (XRD) patterns were recorded from a Siemens D500 diffractometer equipped with a Cu Kα radiation (λ = 0.154 nm). The hydrodynamic diameters of zeolite particles in suspensions were measured with a Malvern Zetasizer Nano ZS equipment at Core Facility of Instrumental BioAnalysis in Laboratory of Bionanotechnology (ICBFM SB RAS, Novosibirsk, Russia). The chemical composition of the samples was determined by inductively coupled plasma optical emission spectrometry (ICP-OES). The samples for ICP-OES were prepared by dissolving 0.1 g of Fe-silicalite in the acid mixture containing 2 m L of 40 wt. % HF and 3 mL of 45 wt.% H_2SO_4 and boiling the mixture for 5 h to remove SiF_4, followed by adding 8 mL of 18 wt.% HCl and bringing the sample volume to 100 mL. Scanning electron microscopy (SEM) images were taken with a JEOL JSM-6460LV microscope at an operating voltage of 15–20 kV. Energy Dispersive X-ray Spectrometry (EDS) and transmission electron microscopy (TEM) images were

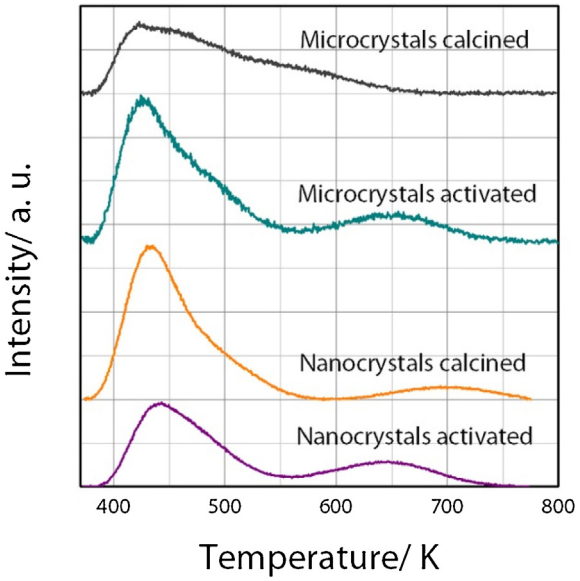

Fig. 7. Profiles of ammonia temperature-programmed desorption from Fe-silicalites.

obtained by a JEOL JEM-2010 microscope operating at 200 kV. Nitrogen adsorption-desorption isotherms were measured with a Quantachrome Autosorb-6B-Kr surface area analyzer at 77 K. Prior to analysis, samples were outgassed at 573 K for 10 h. Specific surface areas were determined applying BET equation [17]. Pore size distributions were estimated by the BJH method [18]. Micropore volume and external surface area were also calculated by means of αs—method with using the isotherm of adsorption of N_2 on the reference LiChrospher Si-1000 silica gel, reported in literature [19,20]. UV–vis diffuse reflection (DR) spectra were recorded on a Shimadzu UV-2501 PC in wavenumber range 11000–54000 cm^{-1} at 298 K. The acidities of the samples were measured by TPD of ammonia in using lab-scale calibrated equipment. Ammonia quantity signal was measured by the quadrupole mass spectrometer HiCube RGA100 and temperature control was operated by temperature controller Termodat 13KT2/5 T supplying continuous sample heat rate.

2.4. Catalytic experiments

Fe-silicalite catalysts were tested in H_2O_2 decomposition in a 5 mL thermostatted glass batch reactor agitated with a magnetic stirrer. Kinetic curves of O_2 emission were recorded by the barometric equipment under the following conditions: the volume of the liquid phase was 2.5 mL, catalyst concentration—20 g L^{-1}, T = 293–333 K and the initial concentration of H_2O_2 was 1 M.

For measuring the H_2O_2 decomposition rate in the filtrate, the catalyst suspension was filtered in 10 min after beginning the H_2O_2 decomposition at $[H_2O_2]_0$ = 1 M, [catalyst] = 20 g L^{-1}, T = 303 K. Then 2.5 mL of the filtrate were placed into the thermostatted reactor equipped with barometric equipment, where the O_2 released pressure was measured.

Total catalytic oxidation of disodium ethylenediaminetetraacetate (Na_2EDTA) by hydrogen peroxide was carried out in a 100 mL thermostatted glass batch reactor agitated with a magnetic stirrer. In the experiment, volume of the liquid phase was 50 ml, catalyst concentration—20 g L^{-1}, T = 293–333 K, initial concentrations of H_2O_2 were 0.1–4 M and initial Na_2EDTA concentration was 1.68 g L^{-1}. We measured kinetic curves of dissolved organic carbon elimination with a total organic carbon (TOC) analyzer (Shimadzu) and mass spectrometer HiCube RGA100. Catalysts regeneration was carried out by rinsing with distilled water, drying and calcination at 773 K for 3 h. pH changing during EDTA oxidation was controlled by pH-meter HI 2221 (Hanna).

Co(II)-EDTA complex was obtained by mixing equimolar quantities of $^{60}Co(NO_3)_2$ diluted with $Co(NO_3)_2$ and Na_2EDTA. Oxidation experiments were carried out in glass batch reactors agitated with a magnetic stirrer under the following conditions: volume of the liquid phase was 12.5 mL, radiolabeled Co(II)-EDTA complex concentration – 2.5×10^{-3} M, the initial H_2O_2 concentration was 1 M, catalyst concentration – 20 g L^{-1}, T = 298 K. After 90 min of the reaction, cobalt was removed by precipitation at pH 11 followed by centrifugation at 6800 × g for 30 min. The adsorption experiments were carried out by the same way but without H_2O_2 addition, blank experiments—without H_2O_2 and catalysts. The radioactivity of solutions was measured by gamma-ray spectrometer ATOMTEX МКС-1315.

3. Results and discussion

We have synthesized two materials consisting of Fe-silicalite crystals with different size referred to as nanocrystals and microcrystals. Fe-silicalite nanocrystals have a narrow size distribution and an average size of 190 nm and spheroidal shape according to dynamic light scattering and transmission electron microscopy, respectively (Fig. 1).

Fe-silicalite microcrystals show a wide crystal size distribution from 2 to 10 μm and various morphologies including spheroidal and coffin-like shapes (Fig. 2e, f). Both Fe-silicalite nanocrystals and microcrystals mainly form aggregates built of closely packed crystals after the centrifugation followed drying and calcination, while the single crystals can be also found by SEM (Fig. 2).

One half of calcined Fe-silicalites was left in the calcined form, whereas the other half was activated by acid treatment followed by calcination. The aim of the activation was to form active sites—iron oxide clusters [21]. Fe-silicalites have XRD patterns typical for MFI structure [22] and high crystallinity (Fig. 3). We evaluated the relative crystallinity degree by the integration of peaks in the range from 22.5 to 25° relative to calcined Fe-silicalite microcrystals under identical). The activation of Fe-silicalites by oxalic acid treatment followed by calcination resulted in small crystallinity decreasing because of defects formation. 10 cycles of EDTA oxidation, when each cycle followed by regeneration *via* rinsing with distilled water, drying and calcination, resulted in 10–30% crystallinity decreasing, the highest decrystallization referring to activated Fe-silicalite nanocrystals (Fig. 3, Table 1).

Textural characteristics of Fe-silicalite materials determined by the nitrogen adsorption can be seen in Table 1. All Fe-silicalite samples exhibit high BET surface areas (398–480 m^2 g^{-1}) and micropore volumes (0.11–0.12 cm^3 g^{-1}). The external surface area and total pore volume of Fe-silicalite nanocrystals are much higher than those one of microcrystals.

Nitrogen adsorption/desorption isotherms and pore size distributions of zeolite materials are presented in Fig. 4. For all samples, isotherms have a clear uptake at low relative pressure corresponding to filling micropores with nitrogen. In case of Fe-silicalite microcrystals, isotherms show the initial step increase followed by horizontal adsorption and desorption branches, referring to the Type I isotherm, typical for microporous materials. For Fe-silicalite nanocrystals, isotherms exhibit the hysteresis loop at high relative pressure ranges indicating the presence of large mesopores between closely packed particles. Mesopore size distributions estimated by the BJH method are shown in Fig. 4b. Distribution curves for Fe-silicalite nanocrystals show a sharp maximum at 28 nm confirming close packing of particles in the bulk. Fe-silicalite micro-

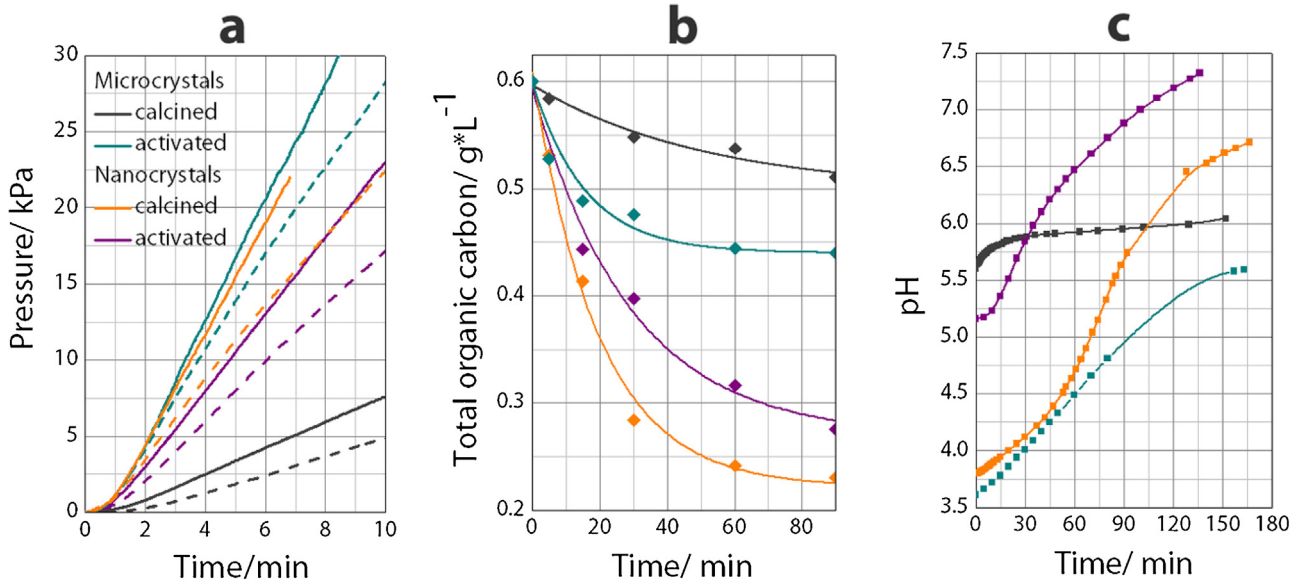

Fig. 8. The kinetic curves of the O_2 release (a) and EDTA mineralization (b) from 20 g L^{-1} Fe-silicalite suspensions without EDTA (solid lines) and with EDTA (dash lines). Kinetic curves of pH changing during EDTA oxidation (c). T = 303 K, $[H_2O_2]_0$ = 1 M, $[Na_2EDTA]_0$ = 1.68 g L^{-1}, [catalyst] = 20 g l^{-1}.

crystals contain a bit of mesopores in the range 10–20 nm seemed to be structural defects.

The iron content in Fe-silicalites measured by the chemical analysis can be found in Table 1. The iron quantity is the same for calcined Fe-silicalite nano- and microcrystals. After the activation procedure consisting of the oxalic acid treatment followed by drying and calcination, iron amount decreased in case of nanocrystals resulting from higher accessibility of iron species for oxalic acid in case of smaller crystals. The iron leaching under EDTA oxidation followed by regeneration amounts to 6–9% and 10–15% after 5 and 10 catalytic cycles, respectively (Table 1).

The state of iron species in as-synthesized, calcined and activated Fe-silicalite materials was studied by UV–vis DR spectroscopy. A strong absorption in the 30 000–50 000 cm^{-1} region was observed for all materials. Absorption bands around 41 000 and 46 000 cm^{-1} correspond to O^{2-} ligand → metal charge transfer $t_1 \rightarrow e$ and $t_1 \rightarrow t_2$ involving Fe^{3+} in tetrahedral or octahedral oxygen surroundings. Spectra for as-synthesized Fe-silicalites exhibit three extremely weak peaks around 22 900, 24 500 and 26 800 cm^{-1} (Fig. 5) referring to forbidden d–d transitions $^6A_1 \rightarrow {}^4T_1$, $^6A_1 \rightarrow {}^4T_2$, and the sum of $^6A_1 \rightarrow {}^4A_1$ and $^6A_1 \rightarrow {}^4E$ of isolated high spin Fe^{3+} ions in tetrahedral oxygen coordination. UV–vis DR spectra of white as-synthesized Fe-silicalites confirm that Fe^{3+} ions occupy tetrahedral lattice positions [23].

In UV–vis DR spectra of calcined and activated Fe-silicalites, intensive absorption peaks have arisen at 31 000–33 000 cm^{-1} indicating clusters formation with Fe^{3+} in octahedral complexes [23,24]. Calcination resulted in partial Fe^{3+} migration from the zeolite lattice to form small clusters of iron species in extra framework positions. The absorption bands of iron oxide clusters inside Fe-silicalite nanocrystals have about 2000 cm^{-1} shift to blue *vs.* microcrystals due to increasing the Fe_2O_3 band gap resulting from the size quantization effect (see ESI Fig. 1a) [25].

Actually, TEM visualization shown that iron species inside nanocrystals were less than 1 nm in size, while Fe-silicalite microcrystals contain larger ferric particles in the range of 3–4 nm located inside mesopores or on crystals surface (Fig. 6).

The following Fe-silicalite microcrystals activation induced further iron species migration followed by their aggregation confirming by the absorption band emergence at 33 000 cm^{-1}, while no additional bands was observed after the activation of nanocrystals (see ESI Fig. 1b). To sum up, the calcination is sufficient for the maximum activation of Fe-silicalite nanocrystals, namely the formation of maximum quantity of ferric clusters, while the additional acid treatment is required for the greatest microcrystals activation.

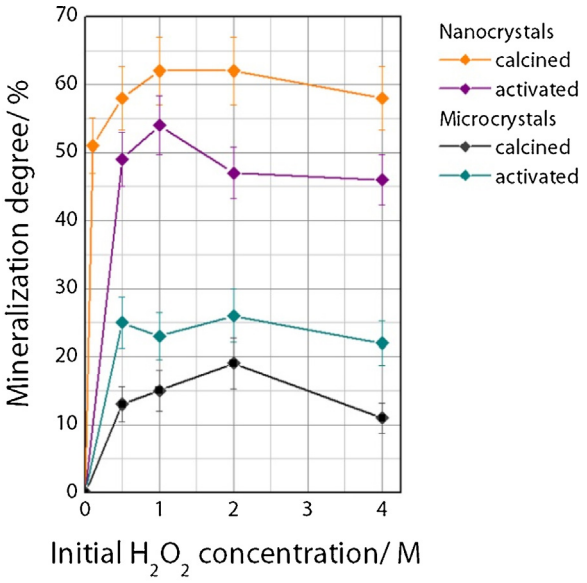

Fig. 9. The dependence of the EDTA mineralization degree on the H_2O_2 initial concentration at [catalyst] = 20 g L^{-1}, $[EDTA]_0$ = 1.68 g L^{-1}, T = 303 K.

After 10 cycles of EDTA oxidation followed by the catalysts regeneration, the characteristic absorption bands for iron oxide clusters partially disappeared and at the same time weak peaks referring to forbidden d–d transitions were shown up again in spectra of used catalysts. Moreover visible changes have occurred with the samples color, it changed from light beige to white, also indicating almost total iron oxide clusters leaching. Taking into account the changes in elemental composition, described above, one can see the high stability of framework iron, however, lattice ions are practically inactive in EDTA oxidation. It is iron oxide clusters that are mainly responsible for the catalytic activity (Tables 2 and 3). It is worth noting that only 15–16% of lattice ions was possible to trans-

Table 2
Catalytic performance of Fe-silicalites. $[H_2O_2]_0 = 1$ M, [catalyst] = 20 g L^{-1}, $[EDTA]_0 = 1.68$ g L^{-1}.

Fe-silicalite sample	Initial H_2O_2 decomposition rate (W_0), $mgO_2\ min^{-1}$ $[EDTA]_0 = 0$, $T = 303$ K	Initial H_2O_2 decomposition rate (W_{EDTA}), $mgO_2\ min^{-1}$ $[EDTA]_0 = 1.68$ g L^{-1} $T = 303$ K	$(W_0 - W_{EDTA})/W_0$,%	Initial EDTA oxidation rate, mg carbon/min $T = 303$ K	ΔpH in 90 min of EDTA oxidation $T = 303$ K	E_a for EDTA oxidation, kJ mol^{-1}	E_a for H_2O_2 decomposition, kJ mol^{-1} $[EDTA]_0 = 0$
Microcrystals calcined	0.014	0.010	27	0.002	0.34	34 ± 6	53 ± 1
Microcrystals activated	0.077	0.051	34	0.008	1.32	62 ± 5	68 ± 2
Nanocrystals calcined	0.061	0.044	28	0.014	1.92	53 ± 3	70 ± 2
Nanocrystals activated	0.041	0.032	23	0.009	1.53	41 ± 3	84 ± 5

Table 3
Stability of Fe-silicalite catalysts. $[H_2O_2]_0 = 1$ M, [catalyst] = 20 g L^{-1}, $[EDTA]_0 = 1.68$ g L^{-1}, $T = 303$ K.

Fe-silicalite sample	EDTA conversion in 1.5 h,% (1 cycle)	EDTA conversion in 1.5 h,% (5 cycle)	EDTA conversion in 1.5 h,% (10 cycle)	H_2O_2 decomposition rate after the catalyst filtration, $mgO_2\ min^{-1}$
Microcrystals calcined	15 ± 2	14 ± 2	6 ± 2	7.8×10^{-5}
Microcrystalsactivated	22 ± 3	22 ± 3	2 ± 2	1.2×10^{-5}
Nanocrystals calcined	61 ± 5	56 ± 4	3 ± 2	3.4×10^{-4}
Nanocrystals activated	53 ± 4	17 ± 2	6 ± 2	1.6×10^{-4}

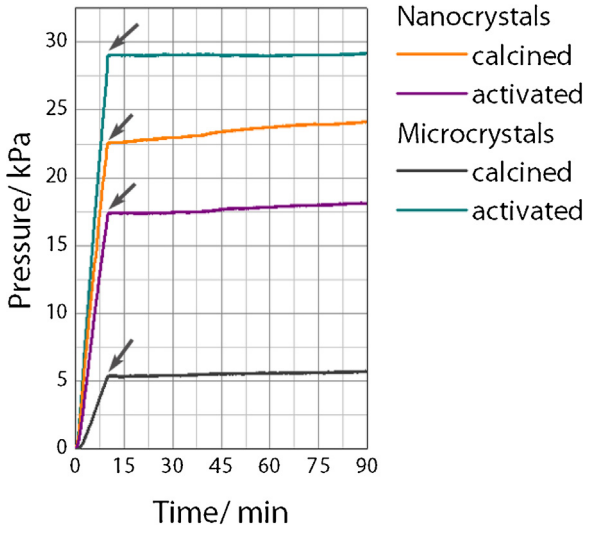

Fig. 10. The kinetics of the O_2 release from the 20 g L^{-1} Fe-silicalite suspensions and their filtrates. Filtration time = 10 min, $T = 303$ K, $[H_2O_2]_0 = 1$ M. The arrows show the moment of filtration.

form to active iron clusters by the acid activation of Fe-silicalite microcrystals and the calcination of nanocrystals, the further activation of nanocrystals resulted mainly in the iron clusters leaching (Table 3).

The acidity of Fe-silicalite materials was measured by means of temperature programmed desorption (TPD) of ammonia. The TPD spectra of ammonia for all Fe-silicalites exhibit low temperature peak (l-peak) at about 430 K (Fig. 7). For Fe-silicalite nanocrystals, high temperature peaks (*h*-peaks) are at 700 and 645 K in case of calcined and activated samples, respectively. The shift of *h*-peak to lower temperature and the disappearance of the strongest acid sites after acid treatment of calcined Fe-silicalite nanocrystals seems to be caused by partial Fe^{3+} migration from the lattice positions, producing extraframework Fe^{3+} ions, iron oxide clusters and structural defects. Actually, the acid strength depends on the surroundings of trivalent cations including the chemical composition and structure of zeolite [26,27]. The same decreasing of the strength and number of acidic sites has already observed earlier after the steam treatment of FeZSM-5 [28–30]. Decreasing the acid strength may be resulted from the substitution of protons by extraframework Fe^{3+} ions [31]. For FeZSM-5 synthesized by ion exchange technique, the higher the iron content, the lower the number of strong acid sites and the higher the number of middle or/and weak acid sites [32,33], apparently arising from increasing extraframework Fe^{3+} content.

On the contrary, there is no *h*-peak in TPD profile for calcined Fe-silicalite microcrystals, while long shoulders stretching from *l*-peak to 650 K can be clearly observed. This shoulder seemed to be the superposition of the peaks referring to acid sites with the middle strength. After activation, high temperature peak at 647 K were observed in TPD profiles. Strong acid sites were formed because of H^+ exchange into Na-form Fe-silicalite under the acid treatment followed by calcination. It should be mentioned that Fe-silicalite microcrystals were synthesized using NaOH and TPABr, while only TPAOH was applied for producing Fe-silicalite nanocrystals. Thus, calcined Fe-silicalite nanocrystals were initially in H-form, while calcined microcrystals—in Na-form. For ZSM-5 in Na-form, the absence of the strong acid sites is the regular phenomenon [34,35]. The total NH_3 adsorption capacity of zeolites were calculated by integrating the area under the TPD profiles (see Table 1), capacity values directly correlating with initial pH of Fe-silicalite suspensions under EDTA oxidation (see Fig. 8c). Kinetic curves of O_2 emission during H_2O_2 decomposition using Fe-silicalites in presence and absence of EDTA are shown on Fig. 8a. The initial parts of kinetic curves have induction periods indicating free-radical H_2O_2 decomposition mechanism [36]. This fact can be also confirmed by high values of apparent activation energies of H_2O_2 decomposition in the range from 53 to 84 kJ Mol^{-1} (see Table 2) as expected at pH values from 3.5 to 7 (Fig. 8c) [36].

The values of initial reaction rates at 303 K and apparent activation energies of hydrogen peroxide decomposition are presented in Table 2. The activities of calcined Fe-silicalite nanocrystals at 303 K are 4.3-fold higher compared with calcined microcrystals most probably due to the higher amount of catalytically active iron oxide clusters in nanocrystals *vs.* microcrystals.

The apparent activation energies for the H_2O_2 decomposition in case of calcined micro- and nanocrystals are 53 ± 1 and 70 ± 2 kJ Mol^{-1}, respectively. We have also determined Ea for H_2O_2 decomposition in homogeneous system $Fe(NO_3)_3/H_2O_2$ at pH_0 2.5 and it equals 84 ± 4 kJ Mol^{-1}. The apparent activation energy

Table 4
^{60}Co removal efficiency. [Catalyst] = 20 g L^{-1}, $[H_2O_2]_0$ = 1 M, $[^{60}Co(II)\text{-}EDTA]_0 = 2.5 \times 10^{-3}$ M, T = 298 K.

Calcined Fe-silicalite sample	The oxidation experiment			The blank experiment		
	Radioactivity, Bq		Cobalt removal, %	Radioactivity, Bq		Cobalt removal, %
	Before	After		Before	After	
Microcrystals	1848 ± 37	1566 ± 136	15 ± 9	1725 ± 82	1794 ± 48	0
Nanocrystals	1937 ± 88	1421 ± 155	27 ± 12			

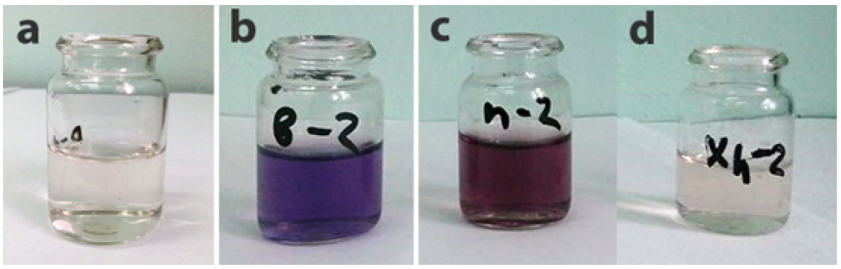

Fig. 11. ^{60}Co-EDTA solutions before (a) and after treatment *via* catalytic oxidation by H_2O_2 using Fe-silicalite microcrystals (b) and nanocrystals (c) followed by the cobalt precipitation at pH 11 and separation by centrifugation. $[H_2O_2]_0$ = 1 M, $[^{60}Co(II)\text{-}EDTA]_0 = 2.5 \times 10^{-3}$ M, [catalyst] = 20 g L^{-1}, T = 298 K. ^{60}Co-EDTA solution after the blank experiment: the alkalization up to pH 11 and then centrifugation (d).

decreasing in case of Fe-silicalite microcrystals *vs.* Fe-silicalite nanocrystals and homogeneous Fe(III) appeared to be resulted from the H_2O_2 diffusion contribution to the reaction rate (see ESI). The same correlation was found for the catalytic alkylation of benzene with ethane, the apparent activation energy of the reaction for the conventional and mesoporous zeolite catalysts were 59 and 77 kJ/mol, respectively [37]. For EDTA oxidation, we have observed the lower activation energy in case of activated nanocrystals *vs.* activated microcrystals and calcined nanocrystals (see Table 2). This phenomenon is likely to be the result of the different location of iron oxide clusters inside Fe-silicalites. As stated above, the acid treatment of calcined Fe-silicalite microcrystals induced the iron species migration, while the activation of calcined nanocrystals caused the leaching of active sites. The activation procedure might result in the core-location and shell-location of iron oxide clusters inside activated nano- and microcrystals, respectively. The core-location of active sites inside nanocrystals increases the distance from the adsorbed EDTA to the iron-containing catalytic sites, where •OH radicals are generated, and thicken the layer where •OH radicals interact with H_2O_2, inducing the decrease of the radicals stream to EDTA. Limiting the H_2O_2 decomposition rate by diffusion disappears only in case of activated nanocrystals (Table 2).

The oxalic acid treatment followed by calcination resulted in 5.5-fold increasing the catalytic activity of Fe-silicalite microcrystals in H_2O_2 decomposition, while in case of nanocrystals—1.5-fold decreasing one, because of the leaching of the iron clusters contribute to the decrease in activity of Fe-silicalite nanocrystals after the acid treatment. The apparent activation energies for the H_2O_2 decomposition increased for both nano- and microcrystals after the activation (Table 2) due to the lower diffusion contribution to the reaction rate. Actually the acid treatment induces the defects formation, decreasing diffusion constraints for H_2O_2. The activation process occurs by the following way: the oxalate anions bind iron ions to form complexes followed by their transferring to extra-framework positions or to the acidic bulk solution. Due to high diffusion constraints of iron complexes inside of micro- and mesopores the first ones concentrate inside the crystals and after drying and calcination iron complexes transform to the iron oxide or hydroxide clusters, which are more active compared with framework ions [21]. In case of nanocrystals the acid treatment results in partial leaching of active sites as well as in changing the state of iron sites.

The kinetic curves of EDTA mineralization and pH changing at 303 K can be seen in Fig. 8b, c, and the initial oxidation rates at 303 K are in Table 2. No long induction periods in both EDTA mineralization and H_2O_2 decomposition in presence of EDTA were observed during EDTA oxidation indicating high stability of active sites against complex formation and leaching due to the limited diffusion of EDTA in the microporous Fe-silicalite phase. The higher EDTA mineralization (see Table 2), the higher pH increasing because of the ammonia formation during EDTA oxidation [10]. The difference between O_2 emission rates during H_2O_2 decomposition in the presence and absence of EDTA is in the range 20–35% for all catalysts.

The dependences of EDTA mineralization degrees on the initial hydrogen concentration shown in Fig. 9 had maxima at the initial H_2O_2 concentration about 1–2, further increasing the H_2O_2 concentration did not increase the mineralization degree. For activated Fe-silicalite microcrystals, the mineralization degree was less than 22% despite of the highest activity in H_2O_2 decomposition, while the highest EDTA mineralization degree in the first catalytic cycle was 61% in case of calcined Fe-silicalite nanocrystals. The reason seemed to be the high surface accessibility of Fe-silicalite nanocrystals for substrates resulting in the distance reduction between the organic molecules and the iron-containing catalytic sites, where the •OH-radicals are generated, and thereby increasing the rate of targeting EDTA oxidation by •OH radicals.

We have also carried out the catalytic stability and leaching tests for Fe-silicalite during EDTA oxidation. Fig. 10 shows the kinetic curves of the O_2 emission during the H_2O_2 decomposition in the Fe-silicalite suspensions and in their filtrates during the first catalytic cycle. The catalysts were filtrated in 10 min after starting the reaction during the linear rise of kinetic curves for correct comparing the filtrate and Fe-silicalite activities, the H_2O_2 decomposition rates can be found in Table 3. The contribution of initial H_2O_2 decomposition rates in the filtrate to the total suspension activities do not exceed 0.5% confirming high stability of active sites against leaching during the first catalytic cycle.

However, Fe-silicalite catalysts after the 10-fold use were completely deactivated and practically stopped working, because of leaching iron oxide clusters (see Table 3). As stated above, iron

species inside Fe-silicalites after 10-fold use are mainly inactive lattice ions, which seemed to be less accessible for H_2O_2 and EDTA, as well as for oxidation products resulting from diffusion constraints.

We have carried out the first experiments on ^{60}Co removal from radiolabeled Co(II)-EDTA solution using calcined Fe-silicalite catalysts, the results are presented in Table 4. Co(II)-EDTA adsorption values are within measurement error. Despite of high measuring error, one can see the radiocobalt removal efficiency is twice higher in case of Fe-silicalite nanocrystals *vs.* microcrystals and amounts to 27% because of high external surface accessibility. Total EDTA mineralization degree in case of Na_2EDTA was 60%, radiocobalt appeared to form complexes with products of EDTA oxidation—ethylenediaminediacetates (EDDA), iminodiacetates (IMDA), nitrilotriacetates (NTA), glyoxylates, oxalates, etc [10]. Qualitatively we observed cobalt complexes, ^{60}Co-containing solutions after the treatment were violet and mulberry for microcrystals and nanocrystals, respectively (Fig. 11).

The total EDTA oxidation and complete cobalt removal can be achieved by redosing of hydrogen peroxide. Fe-silicalite catalysts can be used in flow fixed-bed reactor for oxidation of organic compounds in liquid radioactive wastes. The possibilities of the practical implementation of Fe-silicalite/H_2O_2 systems for concentrating the liquid radioactive waste are open for chemical engineers.

4. Conclusions

We have developed a new catalytic method of radiocobalt removal from EDTA chelates. Heterogeneous Fenton-type catalysts consisting of Fe-silicalite crystals with different size have been synthesized. The effect of crystal size and acid activation on catalytic activity and stability in EDTA oxidation has been studied. The iron oxide clusters were shown to be mainly responsible for the catalytic activity, while framework iron turned out to be inactive in EDTA oxidation but highly stable. Only 15% of lattice ions was possible to transform to active iron clusters, however after 10 cycles of EDTA oxidation/catalyst regeneration, iron oxide clusters were leached. The apparent activation energy of H_2O_2 decomposition decreased in case of Fe-silicalite microcrystals *vs.* nanocrystals appeared to be resulted from the H_2O_2 diffusion contribution to the reaction rate. For activated Fe-silicalite nanocrystals, the EDTA mineralization degree was thrice-higher *vs.* nanocrystals due to enhanced catalytic site accessibility. The first experiments on ^{60}Co removal from radiolabeled Co(II)-EDTA solution have shown twice higher removal efficiency in case of Fe-silicalite nanocrystals *vs.* microcrystals. Fe-silicalite nanocrystals are promising for radiocobalt removal from EDTA chelates.

Acknowledgements

The catalysts syntheses was supported by Russian Scientific Foundation (grant 14-13-01155), the catalyst characterization—by Skolkovo Foundation (Grant Agreement for Russian educational organizations no. 3 of 25.12.2014). The authors thank N.A. Rudina, T.V. Larina, S.V. Bogdanov and E.Yu. Gerasimov for their help in the catalyst characterization.

Appendix A. Supplementary data

Supplementary data associated with this article can be found, in the online version, at http://dx.doi.org/10.1016/j.apcatb.2015.12.038.

References

[1] Hyun-Shik Chang, Gregory V. Korshin, John F. Ferguson, Environ. Sci. Technol. 40 (2006) 5089–5094.
[2] James D. Englehardt, Daniel E. Meeroff, Luis Echegoyen, Yang Deng, Françisco M. Raymo, Tomoyuki Shibata, Environ. Sci. Technol. 41 (2007) 270–276.
[3] Patent WO 2007123436, G21F9/12, 01.11.2007.
[4] Patent WO 2009134294, G21F9/08, 05.11.2009.
[5] Patent WO 2009134294, G21F9/08, 05.11.2009.
[6] S. Balaji, V.V. Kokovkin, S.J. Chung, I.S. Moon, Water Res. 41 (2007) 1423–1432.
[7] Jae-Wook Lee, Sang-Joon Chung, Subramanian Balaji, Vasily V. Kokovkin, Il-Shik Moon, Chemosphere 68 (2007) 1067–1073.
[8] Thomas H. Madden, Abhaya K. Datye, Melissa Fulton, Michael R. Prairie, Sabir A. Majumdar, Bertha M. Stange, Environ. Sci. Technol. 31 (12) (1997) 3475–3481.
[9] Eun-Hee Park, Jinho Jung, Hung-Ho Chung, Chemosphere 64 (2006) 432–436.
[10] M. Sörensen, S. Zurell, F.H. Frimmel, Acta hydrochim. hydrobiol. 26 (2) (1998) 109–115.
[11] Kari Pirkanniemi, Sirpa Metsärinne, Mika Sillanpää, J. Hazard. Mater. 147 (2007) 556–561.
[12] Patent WO 2006002054, C02F1/72, 05.01.2006.
[13] Patent WO. 1999021801A1, C02F1/32, 06.05.1999.
[14] Carina A. Emilio, Wilson F. Jardim, Marta I. Litter, Héctor D. Mansilla, J. Photochem. Photobiol. A: Chem. 151 (2002) 121–127.
[15] Mika E.T. Sillanpää, Tonni Agustiono Kurniawan, Wai-hung Lo, Chemosphere 83 (2011) 1443–1460.
[16] Avelino Corma, J. Catal. 216 (2003) 298–312.
[17] S.J. Gregg, K.S.W. Sing, Adsorption, Surface Area, and Porosity, Academic Press, 1982.
[18] E.P. Barrett, L.G. Joyner, P.P. Halenda, J. Am. Chem. Soc. 73 (1951) 373.
[19] J. Landers, G.Y. Gor, A.V. Neimark, Colloids Surf. A 437 (2013) 3.
[20] M. Jaroniec, M. Kruk, J.P. Olivier, Langmuir 15 (1999) 5410.
[21] E.V. Parkhomchuk (Kuznetsova), M.P. Vanina, S. Preis, Catal. Commun. 9 (2008) 381–385.
[22] M.M.J. Treacy, J.B. Higgins, R. Ballmoos, Collection of Simulated XRD Powder Patterns for Zeolites, 3rd. revised ed., Published by The Commission of the International Zeolite Association, 1996.
[23] S. Bordiga, R. Buzzoni, F. Geobaldo, C. Lamberti, E. Giamello, A. Zecchina, G. Leofanti, G. Petrini, G. Tozzola, G. Vlaic, J. Catal. 158 (1996) 486.
[24] J. Pérez-Ramírez, J.C. Groen, A. Brückner, M.S. Kumar, U. Bentrup, M.N. Debbagh, L.N. Villaescusa, J. Catal. 232 (2005) 318.
[25] L.J. Brus, Chem. Phys. 80 (1984) 4403.
[26] Jule A. Rabo, Gregory J. Gajda, Catal. Rev. Sci. Eng. 31 (4) (1989-90) 385–430.
[27] A. Redondo, J. Phys. Chem. 97 (1993) 11754–11761.
[28] J. Pérez-Ramírez, J.C. Groen, A. Brückner, M.S. Kumar, U. Bentrup, M.N. Debbagh, L.A. Villaescusa, J. Catal. 232 (2005) 318–334.
[29] Javier Pérez-Ramírez, Amalia Gallardo-Llamas, J. Phys. Chem. B 109 (2005) 20529–20538.
[30] J. Pérez-Ramírez, G. Mul, F. Kapteijn, J.A. Moulijn, A.R. Overweg, A. Doménech, A. Ribera, I.W.C.E. Arends, J. Catal. 207 (2002) 113–126.
[31] R.Q. Long, R.T. Yang, J. Catal. 198 (2001) 20–28.
[32] Michael Schwidder, M. Santhosh Kumar, Ursula Bentrup, Javier Pérez-Ramírez, Angelika Brückner, Wolfgang Grünert, Microporous Mesoporous Mater. 111 (2008) 124–133.
[33] Jianchao Xia, Dongsen Mao, Bin Zhang, Qingling Chen, Yi Tang, Catal. Lett. 98 (2004) 4.
[34] Yong Tae Kim, Kwang-Deog Jung, Eun Duck Park, Microporous Mesoporous Mater. 131 (2010) 28–36.
[35] James A. Sullivan, Orla Keane, Appl. Catal. B: Environ. 61 (2005) 244–252.
[36] O.A. Makhotkina, E.V. Kuznetsova, S.V. Preis, Appl. Catal. B: Environ. 68 (2006) 85–91.
[37] Christina Hviid Christensen, Kim Johannsen, Iver Schmidt, Claus Hviid Christensen, J. Am. Chem. Soc. 125 (2003) 13370–13371.